RESEARCH ARTICLE SUMMARY

3D GENOMICS

In situ genome sequencing resolves DNA sequence and structure in intact biological samples

Andrew C. Payne*, Zachary D. Chiang*, Paul L. Reginato*, Sarah M. Mangiameli, Evan M. Murray, Chun-Chen Yao, Styliani Markoulaki, Andrew S. Earl, Ajay S. Labade, Rudolf Jaenisch, George M. Church, Edward S. Boyden†‡, Jason D. Buenrostro†‡, Fei Chen†‡

INTRODUCTION: Genomes are spatially organized across length scales from single base pairs to whole chromosomes. This organization is thought to regulate gene expression and control cellular function and varies across cells within organisms. Current methods based on DNA sequencing achieve genome-wide coverage with base-pair resolution but lack spatial context. Alternatively, current methods based on imaging capture spatial context but are targeted and lack base-pair resolution. Thus, a method bridging sequencing and imaging modalities for mapping genome structure is lacking.

RATIONALE: Here, we describe in situ genome sequencing (IGS), a method for simultaneously sequencing and imaging genomes within intact biological samples. Sequencing enables parental alleles and repetitive elements to be distinguished and included in genomic analyses. Further, imaging enables genome-wide study of spatial relationships within cells, such as association of genomic loci with nuclear structures, and between cells, such as structural similarities within cell lineages.

RESULTS: We applied IGS to cultured human fibroblasts and intact early mouse embryos at the pronuclear stage 4 zygote, late two-cell, and early four-cell stages of development, spatially localizing hundreds to thousands of DNA sequences in individual cells. In embryos, we integrated genotype information and immunostaining to identify and characterize parent-specific changes in genome structure between embryonic stages, including parental genome mixing, chromosome polarization, and nuclear lamina association. We further uncovered and characterized single-cell domain structures with lamina-distal boundaries and lamina-proximal interiors in paternal zygotic pronuclei. Finally, we demonstrated epigenetic memory of global chromosome positioning within clonal cell lineages of individual embryos.

CONCLUSION: IGS unifies sequencing and imaging of genomes, offering a method that connects DNA sequences to their native spatial context within and between the cells of intact biological samples. The single-cell domain structures that we observed in zygotes open opportunities for further investigation, including addressing questions about how nuclear structures such as the lamina may modulate the epigenetic or intrinsic domain-forming behaviors of chromatin. Additionally, our observation of epigenetic memory of chromosome positioning highlights how genome organization during mitosis may influence genome structure at later stages of development. We anticipate that further development of IGS and integration with existing in situ molecular profiling technologies will provide increased resolution and enable multiomic measurements, creating new opportunities to study the structure and function of genomes across length scales and organisms. ■

The list of author affiliations is available in the full article online.
*These authors contributed equally to this work.
†These authors contributed equally to this work.
‡Corresponding author. Email: edboyden@mit.edu (E.S.B.); jason_buenrostro@harvard.edu (J.D.B.); chenf@broadinstitute.org (F.C.)

Cite this article as: A. C. Payne *et al.*, *Science* **371**, eaay3446 (2021). DOI: 10.1126/science.aay3446

READ THE FULL ARTICLE AT
https://doi.org/10.1126/science.aay3446

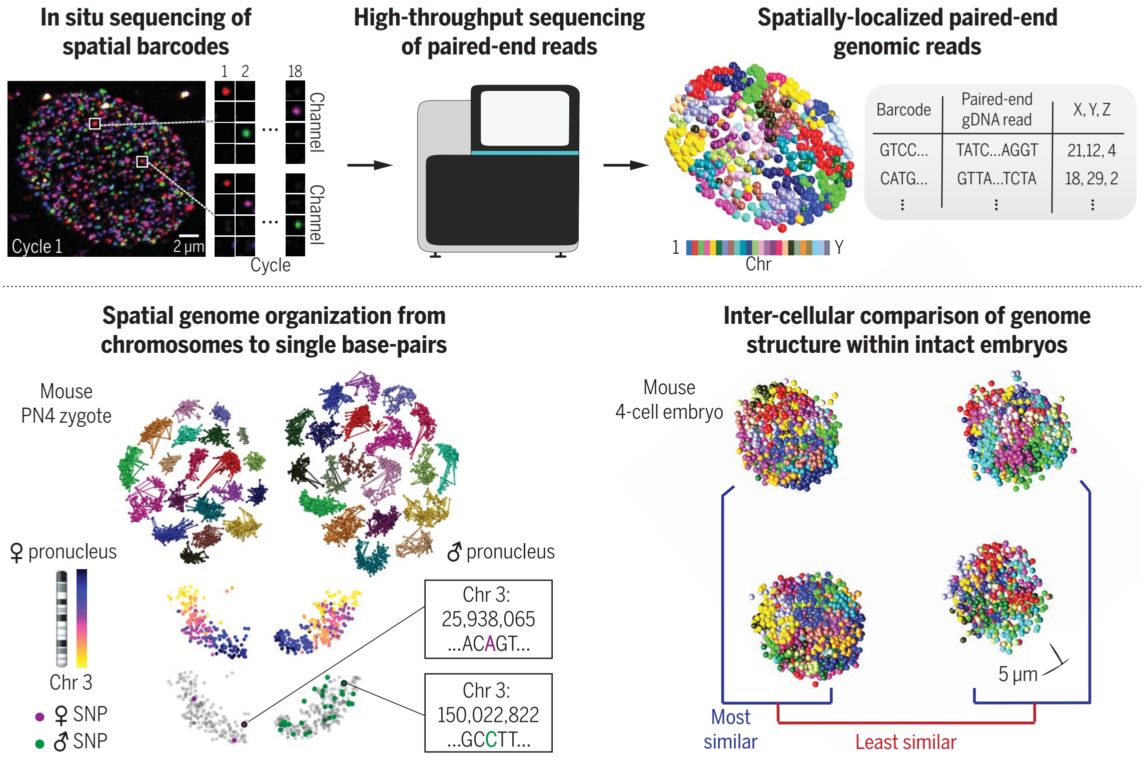

IGS unifies sequencing and imaging of genomes. In situ sequencing of spatial barcodes within intact samples is followed by high-throughput paired-end sequencing. Data from the two modalities are computationally integrated, yielding spatially localized paired-end genomic reads. IGS in early mouse embryos enables the identification of chromosome territories that are assigned to parent-of-origin using base-pair–resolved genotype information. By preserving spatial organization in multicellular samples, IGS allows intercellular comparison of genome structure within individual embryos.

RESEARCH ARTICLE

3D GENOMICS

In situ genome sequencing resolves DNA sequence and structure in intact biological samples

Andrew C. Payne[1,2]*, Zachary D. Chiang[2,3]*, Paul L. Reginato[1,2,4,5,6]*, Sarah M. Mangiameli[2], Evan M. Murray[2], Chun-Chen Yao[2,7], Styliani Markoulaki[8], Andrew S. Earl[3], Ajay S. Labade[3], Rudolf Jaenisch[8,9], George M. Church[5,6], Edward S. Boyden[1,4,7,10,11,12,13]†‡, Jason D. Buenrostro[2,3]†‡, Fei Chen[2,3]†‡

Understanding genome organization requires integration of DNA sequence and three-dimensional spatial context; however, existing genome-wide methods lack either base pair sequence resolution or direct spatial localization. Here, we describe in situ genome sequencing (IGS), a method for simultaneously sequencing and imaging genomes within intact biological samples. We applied IGS to human fibroblasts and early mouse embryos, spatially localizing thousands of genomic loci in individual nuclei. Using these data, we characterized parent-specific changes in genome structure across embryonic stages, revealed single-cell chromatin domains in zygotes, and uncovered epigenetic memory of global chromosome positioning within individual embryos. These results demonstrate how IGS can directly connect sequence and structure across length scales from single base pairs to whole organisms.

The genome of an organism encodes not only its genes but also principles of spatial organization that regulate gene expression and control cellular function (*1*, *2*). Accordingly, mapping spatial genome organization at high resolution is important for understanding its diverse regulatory roles in health, disease, and development (*3*, *4*). Principles of genome architecture have mostly been uncovered by methods based on DNA sequencing of chromatin contacts (*5*), such as Hi-C (*6*), and methods that probe targeted genomic loci using microscopy, such as DNA fluorescence in situ hybridization (FISH) (*7*). Hi-C applied to populations of cells has revealed genome-wide organizing principles (*8*–*12*), and single-cell variations have uncovered cell-to-cell heterogeneity (*13*–*17*). DNA FISH has similarly revealed genome architecture at single-cell resolution (*18*, *19*). More recent studies have shown how these approaches can complement each other by imaging Hi-C–defined features in single cells, characterizing their heterogeneity, and validating inferred differences in chromatin conformation within and across cell types (*20*–*26*).

However, these methods cannot currently be applied jointly on the same cell, and a method to simultaneously sequence and image genomes in single cells is lacking. Efforts that combine Hi-C with microscopy (*16*, *27*) or make FISH more like sequencing through single-nucleotide polymorphism (SNP)–specific probes (*23*, *28*) have broken important conceptual ground, but they remain limited in their imaging or sequencing throughput. Therefore, questions requiring both genomic and spatial analysis in single cells have been difficult to address.

In situ genome sequencing workflow

Here, we present a method for in situ genome sequencing (IGS). IGS enables DNA sequencing directly within intact biological samples, spatially localizing genome-wide paired-end sequences in their endogenous context and thus bridging sequencing and imaging modalities for mapping genomes. Our in situ sequencing workflow introduces innovations in three phases: in situ library construction, multimodal sequencing of libraries, and computational integration of spatial and genetic information.

In the first phase, we created an in situ sequencing library within fixed samples by amplifying an untargeted sampling of the genome in its native spatial context. To do this, we fixed and treated samples using methods optimized for DNA FISH (*28*, *29*). Next, we used Tn5 transposase to randomly incorporate DNA-sequencing adapters into fixed genomic DNA by in situ transposition, preserving genomic fragments in their native spatial positions (*30*). We circularized these fragments in situ by ligation of two DNA hairpins containing a unique molecular identifier (UMI) and primer sites used for subsequent multimodal DNA sequencing (Fig. 1A, ii and iii). We then clonally amplified the resulting circular templates by rolling circle amplification, yielding in situ DNA sequencing libraries with up to thousands of spatially localized amplicons per nucleus (fig. S1). We also developed a method for modulating the effective density of sequencing libraries to optimize the number of resolvable amplicons (fig. S2). These methods provide an approach for clonally amplifying untargeted samples of a genome, creating ~400- to 500-nm-sized features for in situ sequencing (fig. S3).

In the second phase of our workflow, we sought to use reported (*31*) in situ sequencing protocols to determine the sequence and three-dimensional (3D) positions of amplicons. However, current in situ sequencing methods yield short single-end reads (at most 30 bases) and are limited by imaging time (*31*). This poses a challenge for genome sequencing: The human genome encodes 3 billion bases and includes highly repetitive regions, requiring long paired-end sequencing reads to resolve many regions of the genome. To address this challenge, we combined in situ sequencing with high-throughput paired-end DNA sequencing. To do this, we first read amplicon-specific UMIs within fixed samples using sequential rounds of in situ sequencing by ligation (SBL) and fluorescence imaging (*31*) (Fig. 1Bi and movie S1). Immunostaining followed by additional cycles of imaging may also be performed after in situ sequencing. We then dissociated the in situ amplicons and amplified them using polymerase chain reaction (PCR) to produce an in vitro sequencing library (Fig. 1B, ii and iii), which we sequenced on a conventional Illumina sequencer (henceforth referred to as "ex situ sequencing") to obtain 150-bp paired-end genomic reads tagged with in situ sequenced, spatially resolved UMIs. This multimodal sequencing strategy allowed us to preserve spatial information while leveraging the accuracy and read length of paired-end sequencing on the Illumina platform, which is crucial for aligning individual reads to millions of unique genomic loci.

In the third phase, we computationally matched ex situ paired-end sequencing reads to in situ amplicon positions. Briefly, we deconvolved, registered, and normalized fluorescence images to resolve the 3D centers of amplicons across multiple rounds of imaging [fig. S4 (*29*)]. We then quantified the fluorescence signal of each UMI-associated amplicon across four color channels over all rounds

---

[1]Media Arts and Sciences, Massachusetts Institute of Technology (MIT), Cambridge, MA 02139, USA. [2]Broad Institute of MIT and Harvard University, Cambridge, MA 02142, USA. [3]Department of Stem Cell and Regenerative Biology, Harvard University, Cambridge, MA 02138, USA. [4]Department of Biological Engineering, MIT, Cambridge, MA, 02139, USA. [5]Department of Genetics, Harvard Medical School, Boston, MA 02115, USA. [6]Wyss Institute for Biologically Inspired Engineering, Harvard University, Boston, MA 02115, USA. [7]Department of Brain and Cognitive Sciences, MIT, Cambridge, MA 02139, USA. [8]Whitehead Institute for Biomedical Research, Cambridge, MA 02139, USA. [9]Department of Biology, MIT, Cambridge, MA 02139, USA. [10]McGovern Institute, MIT, Cambridge, MA 02139, USA. [11]Koch Institute, MIT, Cambridge, MA 02139, USA. [12]Howard Hughes Medical Institute, Cambridge, MA 02139, USA. [13]Centers for Neurobiological Engineering and Extreme Bionics, MIT, Cambridge, MA 02139, USA.

*These authors contributed equally to this work. †These authors contributed equally to this work.

‡Corresponding author. Email: edboyden@mit.edu (E.S.B.); jason_buenrostro@harvard.edu (J.D.B.); chenf@broadinstitute.org (F.C.)

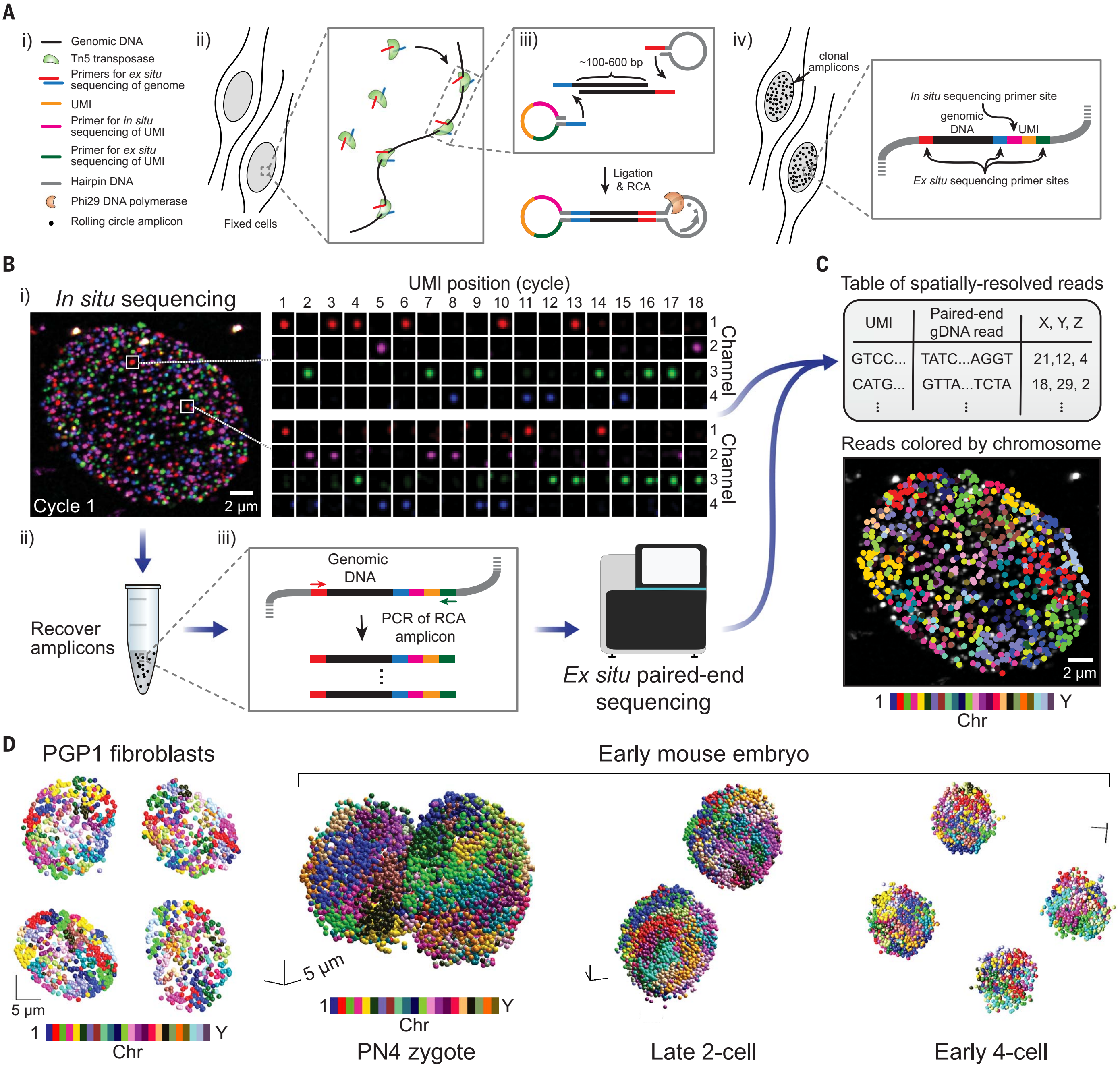

UMI	Paired-end gDNA read	X, Y, Z
GTCC...	TATC...AGGT	21,12, 4
CATG...	GTTA...TCTA	18, 29, 2
⋮	⋮	⋮

Fig. 1. Method for IGS. (**A**) In situ genomic DNA library construction. (i) Legend. (ii) Adapter insertion. (iii) Insert circularization by hairpin ligation, followed by in situ RCA. (iv) Clonal amplicons containing primers for in situ and ex situ sequencing. (**B**) Workflow for IGS. (i) In situ sequencing localizes UMIs. Four-channel imaging of two representative amplicons over 18 rounds of in situ sequencing. (ii) Amplicon dissociation after in situ sequencing. (iii) PCR and ex situ sequencing of amplicons associates genomic sequences with UMIs. (**C**) Top, Paired-end sequences spatially localized by integrating in situ and ex situ sequencing data. Bottom, Matched reads, colored by chromosome, overlaid on their imaged amplicon library (below). (**D**) In situ sequenced nuclei from cultured fibroblasts and intact embryos at the PN4 zygote, late two-cell, and early four-cell stages, with spatially localized reads colored by chromosome.

of in situ sequencing (Fig. 1B, i, and fig. S5). The ex situ–sequenced reads were next associated with spatial coordinates within nuclei through error-robust matching of in situ– and ex situ–sequenced UMIs (Fig. 1C). To do this, we implemented a probabilistic matching approach using principles from single-bit error correction (*32*) (fig. S5). Collectively, the integration of these methods, which include developments across library construction, sequencing, and computational analyses, enables IGS as a general strategy for spatially mapping paired-end reads (*29*).

Here, we applied IGS to 106 human fibroblasts (PGP1f) and 113 cells across 57 intact early mouse embryos at the pronuclear stage 4 (PN4) zygote (n = 24), late two-cell (n = 20), and early four-cell (n = 13) stages of development (Fig. 1D). Across both experiments, 66.35% of clearly resolvable amplicons (87.6% in PGP1f, 61.0% in mouse embryos) were confidently matched to an ex situ genomic read (fig. S6). After cell filtering based on yield, karyotype, developmental stage, and cell cycle (*29*), this yielded a total of 286,335 spatially localized genomic reads (36,602 in PGP1f, table S1; 249,733 in mouse embryos, table S2) with a UMI-matching false discovery rate (FDR) of 0.26% [1.70% in PGP1f, 0.05% in mouse embryo (29)]. Mapped amplicons scaled with nuclear volume, spanning a median of 328 ± 114 reads per nucleus (±SD) in the PGP1f cells, to a median of 3909 ± 2116, 2357 ± 1063, and 1074 ± 622 reads per nucleus in zygote, two-cell-, and four-cell-stage embryos, respectively (fig. S7). Sequencing coverage across the hg38 and mm10 reference genomes was comparable to whole-genome sequencing (fig. S8), and genomic reads did not show bias based on radial position (fig. S9) or chromatin accessibility (fig. S10). We also quantified the rate of detection for each genomic region across individual cells, as well as the distribution of genomic distance between sampled loci on the same chromosome (fig. S11).

For downstream analyses, we annotated each read based on spatial features such as inclusion in chromosome territories and distance to nuclear landmarks (nuclear lamina, centromeres, and nucleolar precursor bodies), as well as published genomic data including A/B compartments, lamina-associated domains, and guanine-cytosine (GC) content (table S3). The full embryo dataset can be interactively visualized at https://buenrostrolab.shinyapps.io/insituseq/.

Validation of IGS in cultured cells

To validate that our method detects features of spatial genome organization, we first examined the locations of chromosomes in interphase human male PGP1 fibroblasts (Fig. 2, A and B, and movie S2). We found that autosomal reads displayed a strong tendency to spatially colocalize into two distinct spatial regions, whereas allosomal reads were restricted to one region, confirming the known organization of chromosomes into territories (18) (fig. S12 and movie S3). To systematically define these territories, we used a maximum likelihood estimation approach to assign reads to homologous chromosome clusters using both the spatial and genomic positions of each read (fig. S13). For chromosomes with two spatially resolved homolog clusters, we found, through density-based thresholding, that 6.83% of reads did not spatially colocalize with either cluster (fig. S13), a larger fraction than our estimated 1.70% UMI-matching FDR in PGP1f, which may be associated with long-range chromosome looping (33). After spatial clustering, we visualized genome-wide conformations of individual chromosomes in single diploid cells by connecting the reads in each cluster according to genomic position (Fig. 2C).

We proceeded to characterize the positions of diploid chromosome territories across single cells by calculating the average spatial distance between pairwise genomic locations across the genome at 10-Mb resolution. We found that blocks of short intrachromosomal distances were strongly delineated along the diagonal of this pairwise distance matrix (Fig. 2D), consistent with genomic organization into chromosome territories described above. The matrix also shows enrichment of shorter pairwise distances between smaller chromosomes. Additionally, we observed a positive association between chromosome size and radial distance from the nuclear center (Fig. 2E). These observations indicate that small chromosomes tend to be in closer proximity near the nuclear center, consistent with prior studies in human fibroblasts (34). These results illustrate the ability of IGS to resolve diploid chromosome territories within the nuclei of single cells and to investigate the spatial positioning of chromosomes at scale.

Repetitive DNA elements, such as transposons and endogenous retroviruses, make up ~50% of the human genome (35, 36), and their localization is known to play a role in normal (37) and disease-associated (38) genome organization. Although FISH-based methods can measure the localization of targeted classes of repetitive sequences (34, 39), current approaches have not simultaneously mapped the localization of many classes of repetitive sequences across the nucleus. We applied IGS to simultaneously measure the localization of repetitive sequences across the genome. We focused on the 13.9% of spatially resolved reads that do not uniquely align to the reference genome (hg38) and aggregated them into ~250 classes of repetitive elements using Repbase (40) (fig. S14A). We found that the number of reads associated with each element was proportional to its observed frequency in hg38 (fig. S14B), enabling an unbiased approach to studying localization of repetitive elements.

Given our observations of radial patterns of chromosome positioning and the known radial organization of heterochromatin (41), we investigated whether repetitive elements displayed radial patterns. To do this, we compared the radial distribution of reads containing repetitive elements with permuted distributions to identify classes of repetitive elements with the strongest radial bias [Fig. 2F (29)]. We confirmed reports that Alu elements are depleted ~1 μm from the nuclear edge (34), further validating our approach (Fig. 2G). We also found that certain types of repetitive heterochromatin, such as satellite DNA, show enrichment toward the nuclear center, whereas others, including AT-rich L1 elements, are overrepresented at the nuclear edge. These findings demonstrate the ability of IGS to simultaneously identify spatial localization patterns of many different repetitive sequences de novo in an untargeted and genome-wide manner.

Having shown that IGS confirms known features of global genome organization, we next investigated whether we could characterize the structures of individual chromosomes. DNA FISH and Hi-C studies have found that chromosome arms can be individually compartmentalized in a fashion similar to chromosome territories (44, 45). Independent localization of chromosome arms was apparent as stripes in the genome-wide distance matrix (Fig. 2D) and could be visualized in single chromosomes colored by their p and q arms (Fig. 2H). We computed pairwise distances for reads within each chromosome territory (Chrs 1 to 11 and Chr X; fig. S15) and fit a power law to this relationship as described previously (20). Separate treatment of the p and q arms resulted in an improved fit compared with fitting of all of Chr 1 (fig. S16), consistent with the expectation of differential scaling across the centromere. Indeed, intra-arm and inter-arm pairs of loci exhibited two scaling regimes when treated separately (Fig. 2I and fig. S17). For chromosomes in which we had high coverage (Chr 1 to 11 and Chr X), inter-arm distances were significantly larger than intra-arm distance for the range of genomic distances present in both distributions [56 to 87 Mb for Chr 1, Fig. 2J; boxed region, Fig. 2I; Kolmogorov-Smirnov (K-S) test, $P < 10^{-16}$, all chromosomes, fig. S18]. These results extend observations of spatially polarized chromosome arms (42) and demonstrate the ability of IGS to characterize subchromosomal spatial structure. These findings highlight the distinctive ability of IGS to simultaneously interrogate broad features of genome organization, including chromosome positioning, chromosome folding, and the localization patterns of repetitive sequences.

IGS in intact early mouse embryos

The spatial organization of the genome is extensively remodeled in early embryogenesis as the initially separate parental genomes undergo major reorganization after fertilization to prime the organism for zygotic genome activation (ZGA) (43) and, subsequently, lineage-specific cell fates (44). Studies have linked chromatin and epigenetic remodeling to various phenomena including sequence-specific localization of chromatin to nuclear landmarks (45, 46), parent-specific chromatin domain organization in single cells (47–50), and developmental specification of clonal lineages (51–53). Given the importance of spatial features, sequence specificity, and intercellular relationships in these phenomena, we sought to apply IGS in intact early embryos to characterize genome organization in early embryogenesis across length scales. We applied IGS to intact early mouse embryos (B6C3F1 females × B6D2F1 males) spanning the PN4 zygote (3909 ± 2116 reads/cell, median ± SD), late two-cell (2357 ± 1063 reads/cell), and early four-cell (1074 ± 622 reads/cell) stages of development (Fig. 3A and movie S4).

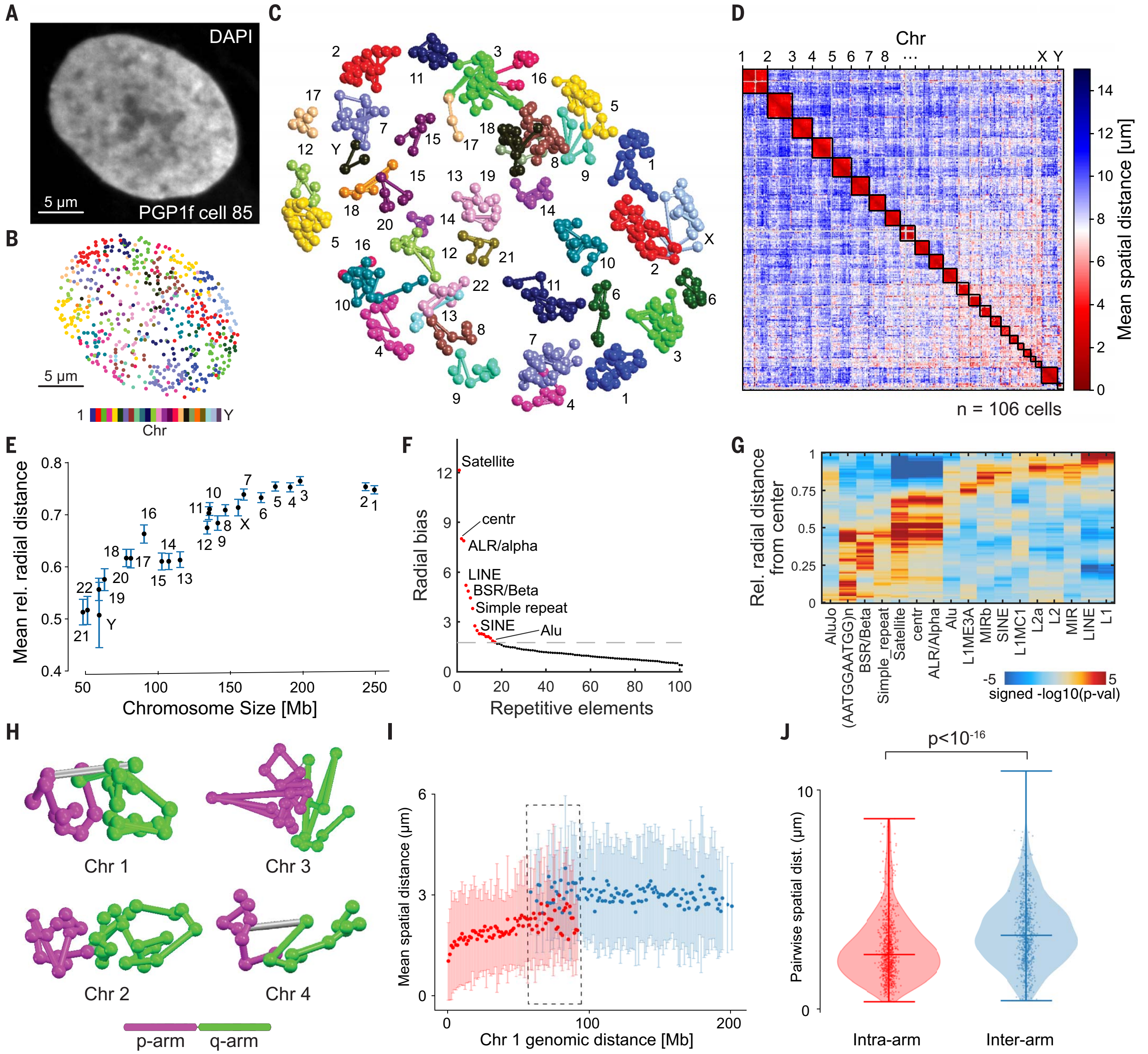

Fig. 2. IGS characterizes spatial features of the human genome. (**A**) DAPI staining of a PGP1f nucleus after in situ library construction. (**B**) Spatially localized reads ($n = 601$) in the same PGP1f nucleus colored by chromosome. (**C**) Exploded view revealing conformations of chromosome territories shown as in situ reads (balls) connected according to sequential genomic position (sticks). (**D**) Genome-wide population mean pairwise distance matrix of 106 PGP1f cells binned at 10 Mb. (**E**) Chromosome size versus normalized mean radial distance from the nuclear center for 106 diploid-resolved PGP1f cells. Error bars denote 95% CI of the mean determined by bootstrapping. (**F**) The 103 most abundant repetitive elements ordered by radial bias, defined as the variability of binned distances relative to a permuted background from the nuclear center for 106 PGP1f cells. The dashed gray line represents the threshold for elements shown in (G). (**G**) Radial enrichment and depletion by binned distance from the nuclear center for the repetitive elements with the strongest radial bias from (F). (**H**) Ball-and-stick models for Chr 1 to 4 in the same single cell, demonstrating spatial polarization between the p and q arms of each chromosome. (**I**) Genomic distance versus spatial distance for Chr 1, distinguishing intra-arm and inter-arm measurements. Error bars indicate SD. Dashed box indicates the range in which both measurements can be compared at reasonable sampling depth ($n > 20$ per 1-Mb bin). (**J**) Intra-arm and inter-arm distance distributions in the dashed range in (I) are distributed differently ($n = 819$ intra-arm, 766 inter-arm, 144 Chr 1 territories, K-S test, $P < 10^{-16}$). Violin plot indicates median and range.

Collectively, imaging and sequencing methods have shown that some of the structural changes in early development are associated with nuclear landmarks such as centromeres (*54*), nuclear lamina (*46*), and nucleolus precursor bodies (NPBs) (*55*). To demonstrate that IGS is compatible with other imaging modalities and to investigate the organizational roles of these landmarks, we performed coimmunostaining for CENP-A (centromere) and Lamin-B1 (nuclear lamina), in addition to staining with 4′,6-diamidino-2-phenylindole (DAPI, used to locate NPBs). The resulting images were segmented and registered to the in situ sequencing data in 3D, enabling us to directly

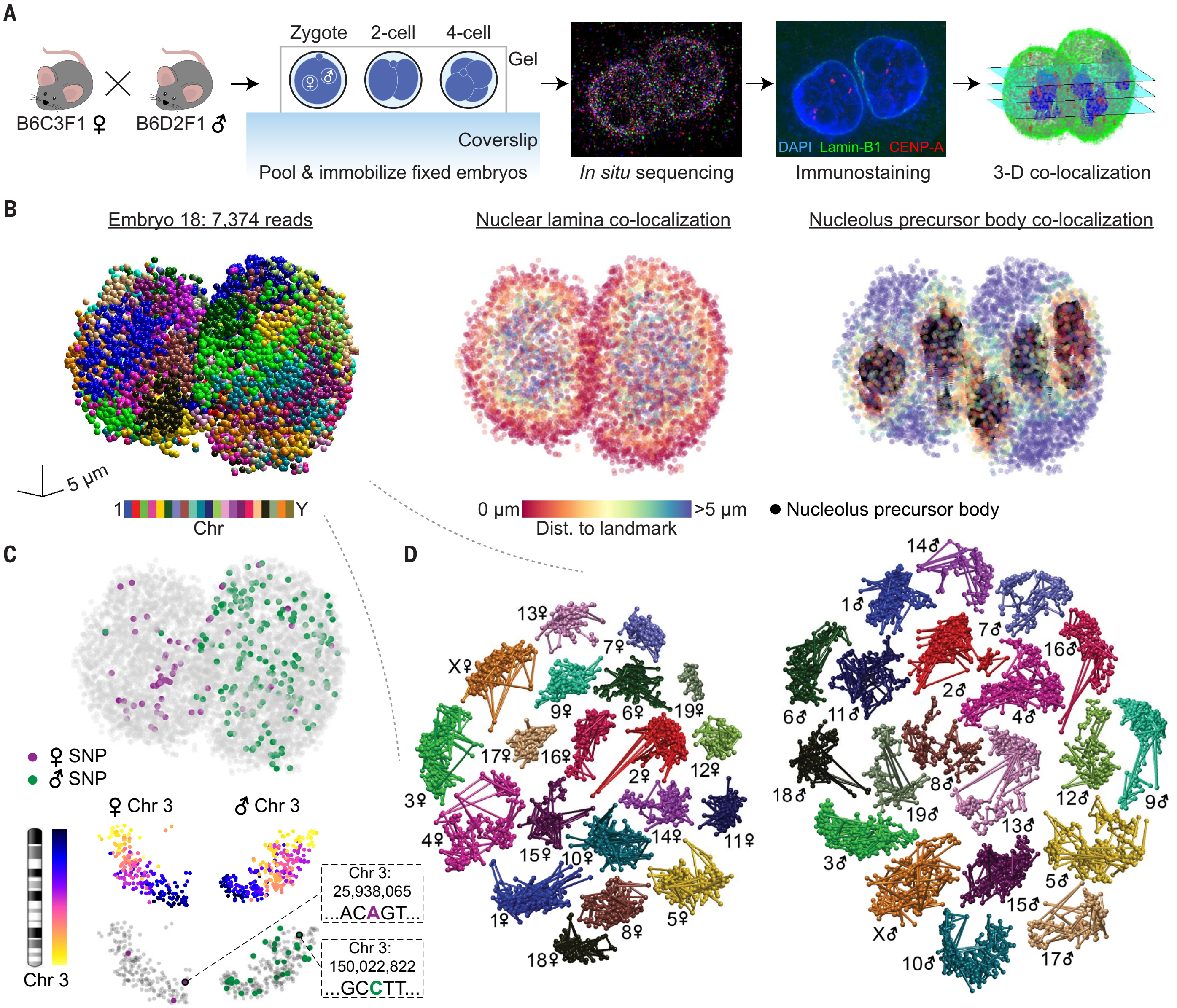

Fig. 3. IGS enables high-resolution genomic and spatial profiling of intact early mouse embryos. (**A**) Workflow. B6C3F1 x B6D2F1 embryos at the PN4 zygote, two-cell, and four-cell stages are pooled, fixed, and immobilized in a polyacrylamide gel. After in situ sequencing, DAPI and immunofluorescence staining of CENP-A and Lamin-B1 are performed. (**B**) Representative zygote with 7374 spatially localized reads colored by chromosome (left), distance to the nuclear lamina (middle), and distance to nearest nucleolus precursor body (right). (**C**) Amplicons from (B), with reads colored by parental haplotype assignment for the intact embryo (top), by genomic position for Chr 3 homologs (middle), and by parental haplotype assignment for Chr 3 homologs (bottom). Boxes show two haplotype-informative Chr 3 SNPs. (**D**) Exploded view of chromosome territories from (B) for the maternal (left) and paternal pronuclei (right).

localize genomic reads relative to these landmarks [Fig. 3B (*29*)].

To resolve the maternal and paternal genomes within single cells, we first confirmed the presence of chromosome territories in all stages. As with the PGP1 fibroblasts, we found that reads originating from a particular autosome could generally be separated into two distinct spatial clusters per nucleus (or one cluster per allosome in male embryos) (movie S5). We then filtered cells based on yield, karyotype, developmental stage, and cell cycle [fig. S19 (*29*)]. After filtering, we found a nearly equivalent rate of reads that did not colocalize with chromosome territories as in PGP1f (6.95%). Relative to reads within territories, these noncolocalizing reads were significantly depleted from regions proximal to the nuclear lamina and NPBs (K-S test, $P < 10^{-51}$ and 10^{-109}, respectively; fig. S20).

To assign parent-of-origin to each territory, we identified spatially localized reads that overlapped a genomic position with a heterozygous SNP in either of the parental strains. We found that 1.40% and 1.64% of genomic reads were uniquely assigned to the maternal (B6C3F1) and paternal (B6D2F1) genomes, respectively, resulting in an average of 67 haplotype-informative reads per cell. To validate these assignments, we visualized the positions of haplotype-informative reads in the PN4 zygote (Fig. 3C). At this stage of development, the parental genomes remain segregated in the larger paternal and smaller maternal pronuclei. On the basis of this known feature, we assigned each chromosome territory to either

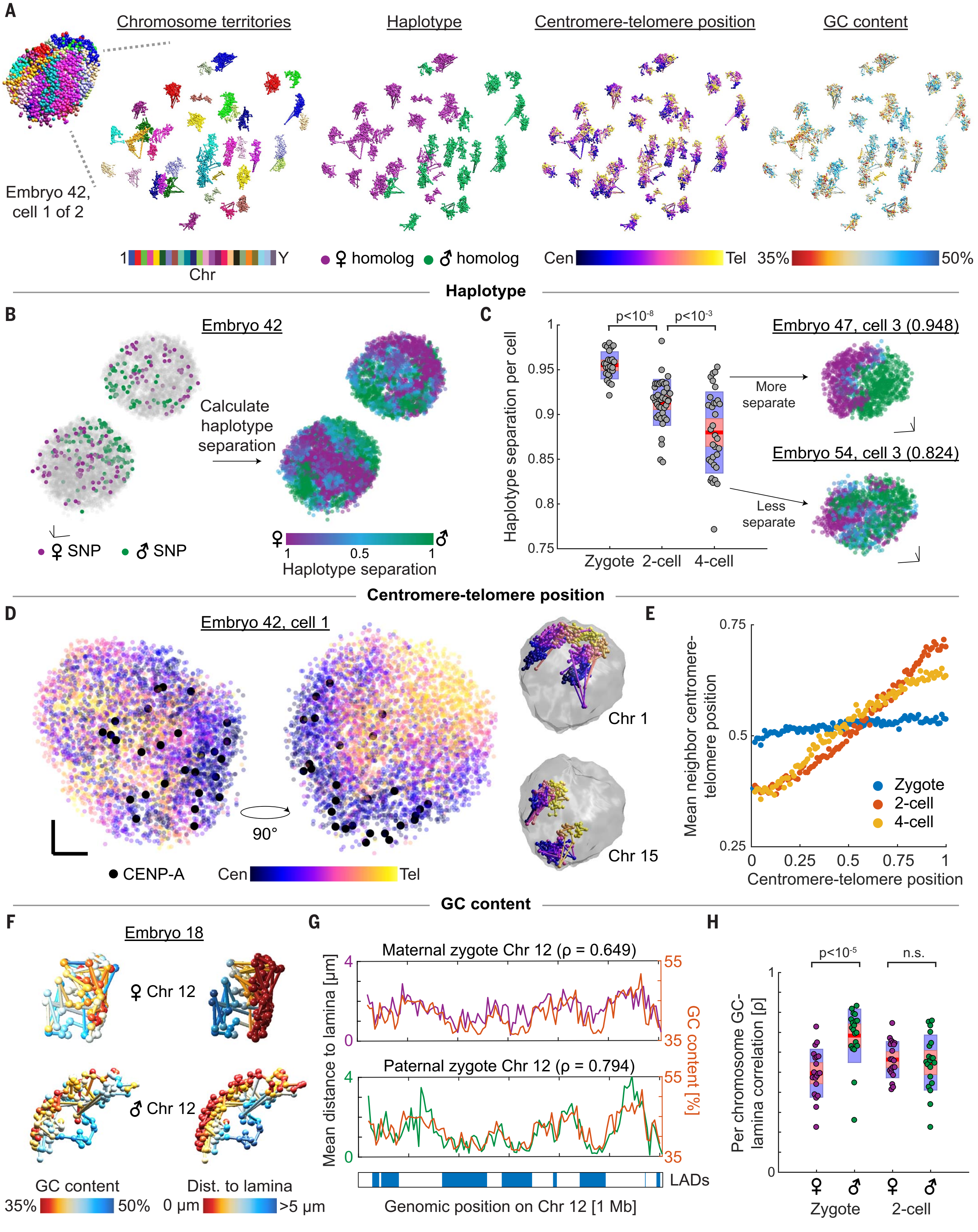
A
Chromosome territories
Haplotype
Centromere-telomere position
GC content
Embryo 42, cell 1 of 2
1
Y
Chr
♀ homolog
♂ homolog
Cen
Tel
35%
50%
Haplotype
B
Embryo 42
Calculate haplotype separation
♀ SNP
♂ SNP
♀
♂
1
0.5
1
Haplotype separation
C
Haplotype separation per cell
1
0.95
0.9
0.85
0.8
0.75
$p<10^{-8}$
$p<10^{-3}$
Zygote
2-cell
4-cell
More separate
Less separate
Embryo 47, cell 3 (0.948)
Embryo 54, cell 3 (0.824)
Centromere-telomere position
D
Embryo 42, cell 1
90°
CENP-A
Cen
Tel
Chr 1
Chr 15
E
Mean neighbor centromere-telomere position
0.75
0.5
0.25
0
0.25
0.5
0.75
1
Centromere-telomere position
Zygote
2-cell
4-cell
GC content
F
Embryo 18
♀ Chr 12
♂ Chr 12
GC content
35%
50%
Dist. to lamina
0 μm
>5 μm
G
Maternal zygote Chr 12 (ρ = 0.649)
Paternal zygote Chr 12 (ρ = 0.794)
Mean distance to lamina [μm]
4
0
4
0
GC content [%]
55
35
55
35
LADs
Genomic position on Chr 12 [1 Mb]
H
Per chromosome GC-lamina correlation [ρ]
1
0
$p<10^{-5}$
n.s.
♀
♂
♀
♂
Zygote
2-cell

Fig. 4. IGS characterizes developmental transitions in embryonic genome organization. (**A**) Exploded view of a single nucleus from a two-cell-stage embryo colored by chromosome territories, haplotype, centromere-telomere position, and GC content. (**B**) Two-cell-stage embryo with spatially localized reads colored by parental haplotype assignment (left) and haplotype separation score (right). (**C**) Boxplots showing mean haplotype separation score per cell across developmental stages (left; K-S test, $P < 10^{-8}$ and $P < 10^{-3}$). Gray dots represent mean scores of single cells. Distribution mean (red line), 95% CI (red box), and 1 SD (blue box) are indicated. Two cells representing extreme scores (>1 SD) are shown (right). (**D**) Nucleus from (A) with spatially localized reads colored by centromere-telomere position, shown from two angles 90° apart (left). Black dots indicate the position of CENP-A as identified from immunostaining. Chr 1 and Chr 15 homologs from this cell are shown (right) to illustrate the Rabl-like configuration. (**E**) Mean centromere-telomere position of spatial neighbors as a function of centromere-telomere position for each stage. (**F**) Chr 12 homologs from a representative zygote with spatially localized reads colored by GC content (left) and distance to lamina (right). (**G**) Plots showing the relationship between GC content and average distance to the nuclear lamina for 1-Mb bins in Chr 12 of the maternal and paternal zygotic pronuclei. Zygotic lamina-associated domains (LADs) defined by DamID are displayed below. (**H**) Boxplots showing Spearman's ρ between GC content and distance to lamina for 1-Mb bins, partitioned by haplotype and developmental stage (K-S test, $P < 10^{-5}$ and n.s.). Dots represent single chromosomes. Distribution mean (red line), 95% CI (red box), and 1 SD (blue box) are indicated. n = 24 zygotes, 40 nuclei from two-cell embryos, and 49 nuclei from four-cell embryos for all panels. Scale bars, 5 μm in all directions.

the maternal or paternal genome in a semi-supervised manner (Fig. 3D). We found that 97.1% of haplotype-informative reads were concordant with this assignment; nonconcordant reads may be attributable to genomic sequencing errors, UMI matching errors, or strain impurities. We then used our haplotype-informative reads to assign entire chromosome territories to parent-of-origin across the two- and four-cell-stage embryos (*29*). This approach enables a strong majority of reads (82.26%), even those not overlapping a SNP, to be assigned to parent-of-origin through colocalization with haplotype-resolved reads in the same territory.

Developmental transitions in embryonic genome organization

Next, we sought to examine previously described principles of global genome organization, focusing on parental haplotype (*56*, *57*), centromere-telomere position (*16*, *54*), and GC content (*6*, *16*) (Fig. 4A).

We began by examining the spatial separation of parental genomes because imaging studies have shown that maternal and paternal chromatin are spatially polarized in early embryos (*56*, *57*). To quantify the spatial separation of parental genomes across developmental stages, we analyzed the spatial interchromosomal neighbors of each read and calculated a haplotype spatial separation score (Fig. 4B). We then averaged the separation scores for all reads in each cell. We found that the mean separation score significantly decreased between the zygote and two-cell stages and between the two- and four-cell stages (K-S test, $P < 10^{-8}$ and $P < 10^{-3}$, respectively; Fig. 4C), consistent with earlier studies (*56*, *57*). The SD of mean separation scores increased with each developmental stage (SD = 0.015 for zygotes, 0.026 for the two-cell stage, and 0.045 for the four-cell stage), indicating that the degree of parental genome intermixing is heterogeneous within the embryo. Further, we observed no evidence that particular chromosomes were more likely to break this separation than others (fig. S21). These results are concordant with the hypothesis that gradual mixing is a consequence of global chromosome repositioning after mitosis.

We next examined global spatial organization of the genome along the centromere-telomere axes of chromosomes. Mouse chromosomes are acrocentric and are known to be arranged in a Rabl-like configuration in early embryos, in which centromeres cluster toward one side of the nucleus and distal telomeres cluster toward the other (*54*, *56*). To confirm this configuration in our data, we first measured the polarity of the CENP-A stain and found that centromeres in the two- and four-cell stages were significantly clustered toward one side of the nucleus (K-S test, $P < 10^{-4}$ and $P < 10^{-8}$). To analyze this configuration for all chromosome positions, we assigned each read a centromere-telomere score based on its genomic position along its chromosome. When we visualized these scores in a nucleus from a two-cell-stage embryo, we observed that the centromere-telomere scores were highly polarized, which was supported by colocalization of the CENP-A immunostaining (Fig. 4D). To quantify this polarization across all stages, we calculated a spatial neighborhood centromere-telomere score for each read (*29*). We then examined the relationship between centromere-telomere scores and neighborhood scores across all reads and observed much stronger correlation in the two- and four-cell stages (Pearson's r = 0.519 and 0.502, respectively) than in the zygote (Pearson's r = 0.074; Fig. 4E). The functional consequences of this transition to a Rabl-like configuration in two- and four-cell-stage embryos remain unclear. In other contexts, this configuration is thought to be an extension of anaphase chromosome positioning into interphase, perhaps without cellular function (*58*). Conversely, it has also been hypothesized to restrict chromatin entanglement (*59*), so it may be involved in constraining genome structure to enable the short cell cycles of the early embryo.

Finally, we examined the role of GC content in genome structure, which is strongly associated with A/B compartmentalization (*6*). To study this effect, we first visualized individual homologs of Chr 12 from zygotic pronuclei (Fig. 4F). We observed that genomic reads from GC-poor regions tended to localize to the periphery of the nucleus, consistent with reports describing the localization of the inactive B compartment (*16*). To quantify this effect, we measured the correlation between GC content and distance to nuclear lamina across Chr 12 in all zygotes and observed that these two factors were correlated in both the paternal and maternal homologs (Spearman's ρ = 0.794 and 0.649, respectively; Fig. 4G). We applied this approach to all chromosomes and found that the paternal homologs were significantly more correlated than their maternal counterparts in the zygote but not in the two-cell stage (K-S test, $P < 10^{-5}$, n.s.; Fig. 4H). This suggests that the degree of GC compartmentalization may be influenced by the differing biological histories of the pronuclei (*47*).

Unexpectedly, when we examined the relationship between genomic position and distance to nuclear landmarks, we observed that Chr X seemed to localize especially far from the nuclear lamina and toward the NPBs in paternal pronuclei (fig. S22). This finding extends models of the role of NPBs in establishing epigenetic asymmetry between parental X chromosomes rapidly after fertilization and in advance of imprinted X inactivation (*45*). These results demonstrate the ability of IGS to characterize 3D genome organization across diverse developmental stages with parent-specific resolution and with respect to nuclear landmarks.

Detection of single-cell chromatin domains in zygotes

Next, we used IGS to examine subchromosomal spatial organization. We focused on our data with the highest genomic resolution, the zygotic pronuclei, in which large-scale, parent-specific reorganization of chromatin is thought to play an important role in ZGA (*60*). First, we characterized the scaling relationship between mean spatial and genomic pairwise distance in the zygotic parental genomes. Consistent with previous reports (*47*), we found that each parental genome had distinct scaling properties (Fig. 5, A and B).

Reports analyzing genome structure in zygotes have suggested that paternal chromatin exhibits unusually weak higher-order structure (>2 Mb) (*47*–*49*). Consistent with these reports,

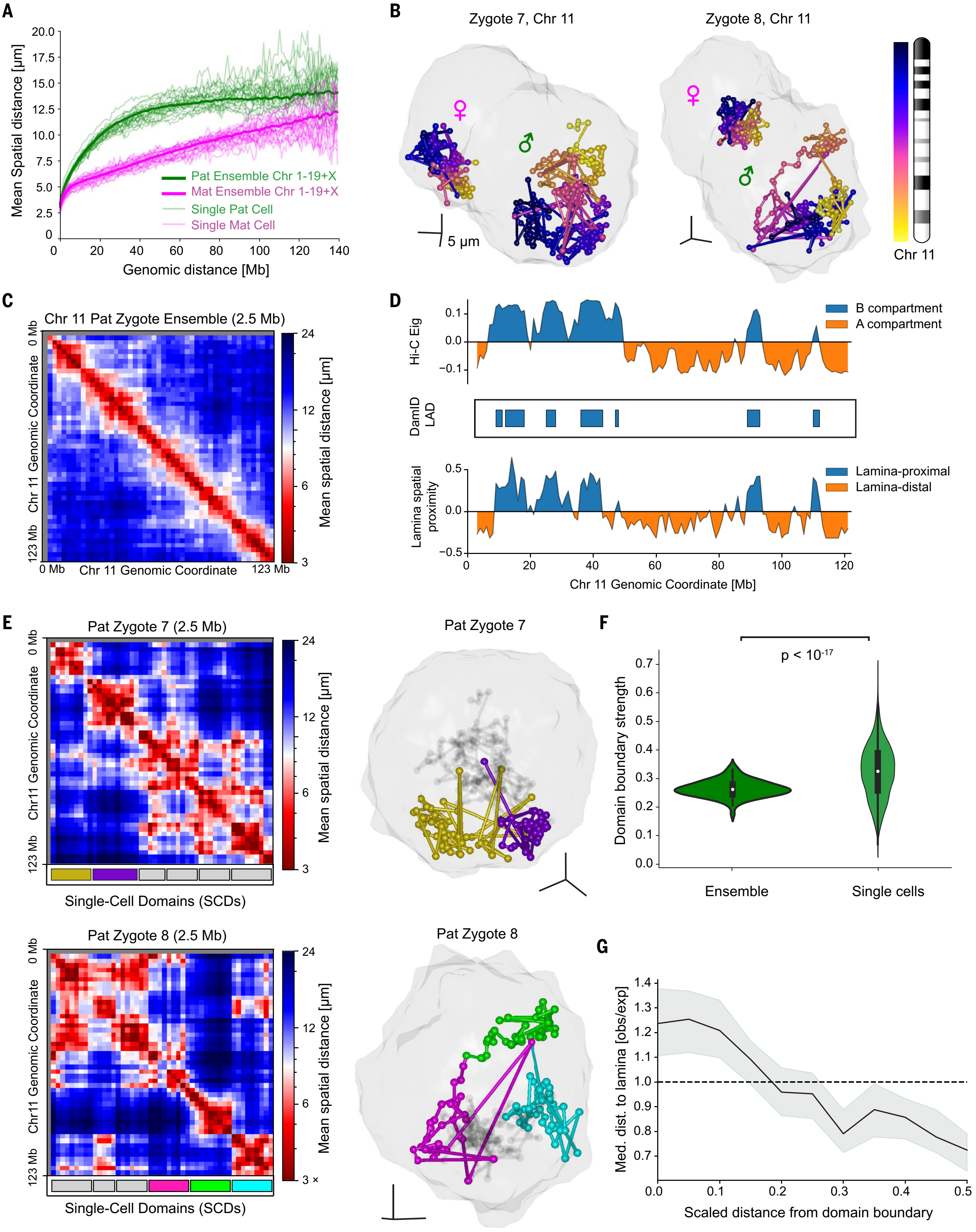
A
Mean Spatial distance [µm]
20.0
17.5
15.0
12.5
10.0
7.5
5.0
2.5
0
0
20
40
60
80
100
120
140
Genomic distance [Mb]
Pat Ensemble Chr 1-19+X
Mat Ensemble Chr 1-19+X
Single Pat Cell
Single Mat Cell
B
Zygote 7, Chr 11
Zygote 8, Chr 11
♀
♂
5 µm
Chr 11
C
Chr 11 Pat Zygote Ensemble (2.5 Mb)
0 Mb
Chr 11 Genomic Coordinate
123 Mb
0 Mb
Chr 11 Genomic Coordinate
123 Mb
24
12
6
3
Mean spatial distance [µm]
D
Hi-C Eig
0.1
0.0
-0.1
B compartment
A compartment
DamID LAD
Lamina spatial proximity
0.5
0.0
-0.5
Lamina-proximal
Lamina-distal
0
20
40
60
80
100
120
Chr 11 Genomic Coordinate [Mb]
E
Pat Zygote 7 (2.5 Mb)
0 Mb
Chr11 Genomic Coordinate
123 Mb
24
12
6
3
Mean spatial distance [µm]
Single-Cell Domains (SCDs)
Pat Zygote 7
Pat Zygote 8 (2.5 Mb)
0 Mb
Chr11 Genomic Coordinate
123 Mb
24
12
6
3
Mean spatial distance [µm]
Single-Cell Domains (SCDs)
Pat Zygote 8
F
p < 10-17
Domain boundary strength
0.7
0.6
0.5
0.4
0.3
0.2
0.1
0.0
Ensemble
Single cells
G
Med. dist. to lamina [obs/exp]
1.4
1.3
1.2
1.1
1.0
0.9
0.8
0.7
0.0
0.1
0.2
0.3
0.4
0.5
Scaled distance from domain boundary

Fig. 5. IGS reveals SCDs in zygotes. (**A**) Global relationship between genomic and spatial distance in zygotes for all chromosomes, distinguishing the parental genomes. (**B**) Visualization of Chr 11 homologs in two zygotes according to parent-of-origin. (**C**) Population ensemble mean spatial distance matrix for paternal Chr 11, constructed at 2.5-Mb resolution (24 zygotic pronuclei, 2317 reads). (**D**) Comparison across measurement modalities for the population of paternal zygotic Chr 11. Top row, Hi-C–defined eigenvalues and compartment calls. Middle row, DamID-defined population lamina-associated domains. Bottom row, lamina-proximal and lamina-distal regions defined with IGS (24 zygotic pronuclei, 2317 reads). (**E**) Top left, Single-cell mean distance matrix for paternal Chr 11 in a representative zygote, with SCD boundaries marked below (263 reads). Top right, Visualization of individual paternal SCDs in the same zygote. To assist visualization, two SCDs are shown in color (purple and gold), whereas the remaining SCDs are shown in gray. Bottom left, Single-cell mean distance matrix for paternal Chr 11 in a second representative zygote, with SCD boundaries marked below (213 reads). Bottom right, Visualization of three paternal SCDs in the second zygote. To assist visualization, three SCDs are shown in color (magenta, lime, and cyan), whereas the remaining SCDs are shown in gray. (**F**) Comparison of single-cell and ensemble domain boundary strengths spanning all detectable boundaries in Chr 1 to 19+X (74 ensemble boundaries, 1057 single-cell boundaries, K-S test, $P < 10^{-17}$). (**G**) Scaled distance from SCD boundary versus observed-over-expected median distance to nuclear lamina, measured genome-wide (Chr 1 to 19+X, $N = 1262$ SCDs). Envelope indicates 95% CI determined by bootstrapping.

we found that spatial distance matrices generated from the population ensemble indeed exhibited little off-diagonal structure (Fig. 5C and fig. S23, all chromosomes). Furthermore, evidence suggests that paternal zygotic chromatin exhibits unusually weak A/B compartmentalization (*47*–*49*) and unusually large lamina-associated domains (*46*). Our ensemble data corroborated these reports and correlated well with Hi-C (mean Pearson's $r = 0.84$) when analyzed in terms of lamina proximity (Fig. 5D and fig. S24, all chromosomes). However, when we examined single-cell distance matrices, we found that, unlike the ensemble, single paternal pronuclei generally exhibited large blocks of spatially associated chromatin (Fig. 5E, left). To distinguish these blocks from population-defined topological domains identified in Hi-C studies, we refer to them as "single-cell domains" (SCDs).

To better understand the nature of SCDs in paternal zygotes, we systematically identified individual domains in single cells (*29*). The SCDs that we identified corresponded well to spatially distinct clusters identified by visual inspection (Fig. 5E, right). When we examined SCDs across cells and chromosomes, we observed that they were large (median size 17.5 Mb, 10 Mb interquartile range) relative to canonical features defined by Hi-C and had heterogeneous sizes and boundary positions (fig. S25). We proceeded to assess the strength of all SCD boundaries in single cells and found they were significantly stronger and more variable than boundaries identified by the same method in the ensemble matrices [K-S test, $P < 10^{-17}$; 95% confidence interval (CI) for Cohen's d (0.56, 0.77) determined by bootstrapping (*29*); Fig. 5F]. These observations suggest that the weak ensemble structure may be explained by the variability of single-cell structures. Finally, we investigated the association of SCDs with nuclear landmarks, which may suggest organizing principles, and found that their boundaries and interiors were, respectively, significantly more lamina-distal and more lamina-proximal than expected [95% confidence interval (CI) determined by bootstrapping, Fig. 5G (*29*)]. We found this interesting in light of previous electron microscopy studies showing discrete, micrometer-scale lamina-associated chromatin domains after ZGA (*61*).

Recently, both polymer simulations (*47*) and direct observation of chromatin structure (*22*) have shown how variable domain-like structures can exist in single cells when higher-order ensemble structure is lacking. We speculate that, given the weak ensemble structure, the SCDs observed here may involve a similar phenomenon. The SCDs described here are larger than canonical Hi-C–defined features and were not detected in earlier single-cell Hi-C studies in zygotes (*47*, *50*), perhaps because they are organized on length scales that are relatively less accessible to Hi-C measurements. It may be interesting to investigate the extent to which SCDs are governed by mechanisms related to the nuclear lamina, which perhaps modulates underlying epigenetic (*41*) or polymer-intrinsic (*47*) domain-forming behaviors of chromatin.

Epigenetic memory of global chromosome positioning within early embryos

Embryonic development is thought to involve epigenetic transmission of structural and regulatory features of chromatin organization through clonal cell lineages within individual embryos (*53*). These mechanisms play an important role in breaking initial symmetry (*51*), in engaging clonal lineage–specific gene expression programs (*62*), and in cell fate commitment (*44*). Intercellular asymmetries influencing the developmental fate of clonal lineages have been reported as early as the four-cell stage within individual embryos (*51*, *52*, *62*, *63*).

To study clonal lineage-specific features at the single-cell level, it is necessary to resolve and compare cells within the same embryo. Chromosome territories have been found to form early in interphase and subsequently maintain their relative positions until prophase (*18*, *64*, *65*), so we reasoned that comparison of chromosome positioning would be a robust way to quantify the similarity of global genome organization between interphase cells. Live-cell studies using nonspecific photopatterning of the nucleus have demonstrated a similarity in global genome organization between sister cells in culture (*65*), and, indeed, visual inspection of pairs of chromosomes suggested that cells within an embryo share similar chromosomal positions (Fig. 6A). We quantified similarity by comparing single-cell autosome distance matrices of pairs of cells within and between individual embryos [Fig. 6, A and B (*29*)]. In two-cell-stage embryos, we found that global chromosome positioning in sister cells was significantly more correlated than in pairs of cells from different embryos (K-S test, $P < 10^{-15}$; Fig. 6C and fig. S26). These results suggest that cells within two-cell-stage embryos may share memory of their common initial chromosome positioning during zygotic metaphase, if not earlier.

Next, we investigated whether the similarity shared by sister cells in two-cell-stage embryos might be epigenetically transmitted across the second cell division, i.e., to cousin cells. Although earlier work did not find heritability in the radial positioning of individual loci (*66*, *67*), widely varying degrees of similarity in global genome organization between mother and daughter cells have been reported (*64*, *65*). We constructed putative clonal lineage trees within each four-cell-stage embryo by using the ranked correlations of autosome distance matrices for each pair of cells to classify putative sister and cousin cells. The most correlated pair of cells in each embryo was designated as one set of putative sister cells, thus implying the remainder of the tree [Fig. 6D and fig. S27 (*29*)]. As expected by the definition of the tree, we found that global chromosome positioning was significantly more correlated between putative sister cells than between pairs of cells from different four-cell-stage embryos (K-S test, $P < 10^{-14}$). However, we also found that the same held true for putative cousin cells, which was not expected [K-S test, $P < 10^{-3}$; 95% CI for Cohen's d (0.55, 1.29) determined by bootstrapping (*29*); Fig. 6E and fig. S26]. These results demonstrate clonal lineage–specific similarity in global chromosome positioning in early embryos and imply that epigenetic memory of chromosome positioning is transmitted from mother to daughter cells during

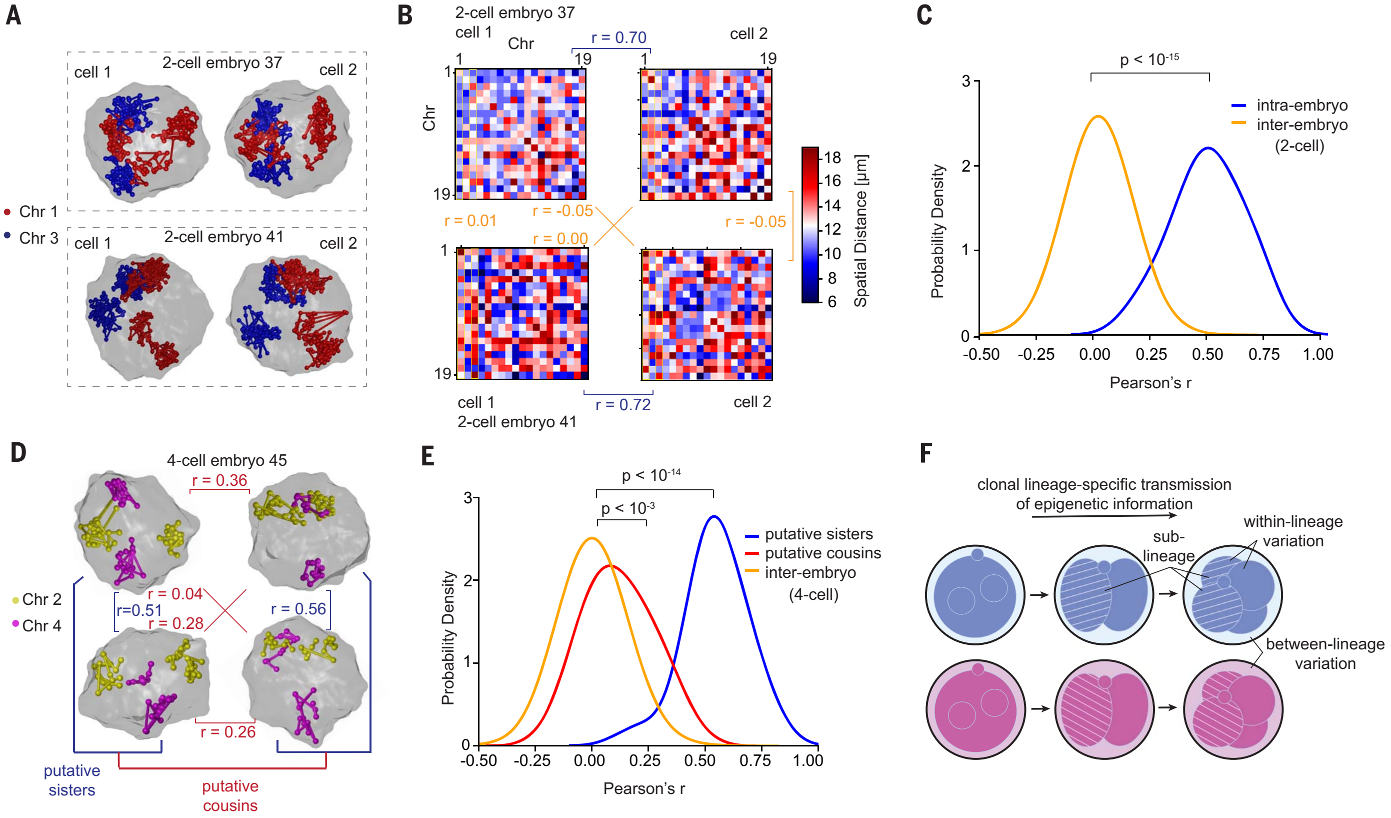

Fig. 6. IGS uncovers epigenetic memory of global chromosome positioning within single embryos. (**A**) Positioning of Chr 1 and 3 in the cells of two-cell-stage embryos 37 (top) and 41 (bottom). (**B**) Pairwise correlations between autosome distance matrices for the cells in (A). Intra-embryo and inter-embryo correlations are shown in blue and orange, respectively. (**C**) Probability distributions of correlations between autosome distance matrices for intra-embryo and inter-embryo pairs of cells among two-cell-stage embryos. K-S test, $P < 10^{-15}$; $n = 20$ intra-embryo pairs and $n = 760$ inter-embryo pairs, among 20 two-cell-stage embryos. (**D**) Positioning of Chr 2 and Chr 4 in the cells of four-cell-stage embryo 45. Pairs of cells are putatively classified as sister and cousin cells based on correlation of global chromosome positioning, with the most correlated pair classified as sisters. Correlations between sister and cousin cells are shown in blue and red, respectively. (**E**) Probability distributions of correlations between autosome distance matrices for pairs of putative sister cells, cousin cells, and inter-embryo pairs of cells among four-cell-stage embryos. K-S test, $P < 10^{-14}$ for sisters versus inter-embryo and $P < 10^{-3}$ for cousins versus inter-embryo; $n = 18$ sister pairs, $n = 36$ cousin pairs, and $n = 933$ inter-embryo pairs, among 13 four-cell-stage embryos. (**F**) Model of epigenetic memory transmission within clonal lineages.

the second cleavage (Fig. 6F). Although the mechanisms are not fully clear, this memory may reflect minimal relative repositioning of chromosomes during congression to and departure from the metaphase plate, perhaps due to the Rabl configuration and short cell cycles of the early embryo. This mitotic heritability of global chromosome positioning may influence processes that affect the viability and phenotype of the developing organism, such as rates of homologous recombination–mediated double-strand break repair (*68*, *69*) and the distribution of translocations (*70*–*72*) in the early embryo.

Discussion

In this work, we present IGS, a method that unifies sequencing and imaging of genomes in intact samples. This unified approach enables de novo discovery of spatial organization of genomes across length scales, from single-cell, subchromosomal domains to intercellular relationships. Because IGS is both sequencing and imaging based, it can be extended in either modality based on the needs of specific experiments. We demonstrate this in early mouse embryos through integration of genotype information to spatially resolve the maternal and paternal genomes by integration of immunofluorescence to localize genomic loci relative to nuclear landmarks and by using whole-embryo spatial information to infer clonal lineages. This contextual information enabled us to uncover single-cell chromatin domains in zygotes with lamina-distal boundary positions and lamina-proximal interiors, as well as heritable correlations in global chromosome positioning within single early embryos.

Whereas extant methods such as multiplexed DNA FISH and single-cell Hi-C are well suited to measuring aspects of spatial genome organization, they cannot currently be combined in the same cell. With IGS, we were able to spatially localize hundreds to thousands of genomic loci in single cells, achieving genomic resolutions comparable to recent genome-wide approaches based on targeted DNA FISH in fibroblasts (*73*, *74*). Unlike these targeted methods, we further show how IGS can perform untargeted sequence localization, resolve genome structure of maternal and paternal alleles, and be applied in 3D nuclei and thick intact samples. However, because of its genome-wide sampling frequency (at most ~1 Mb in this report), IGS is currently limited in its ability to systematically examine specific genetic loci in specific cells. Targeted DNA FISH or single-cell Hi-C are thus currently more appropriate for applications requiring high-resolution interrogation of genomic features such as topologically associating domain boundaries (*22*, *47*, *75*) or enhancer-promoter loops (*16*, *26*), and chromosome-painting methods (*76*) may be preferred when high-throughput visualization of chromosome territories is required.

IGS therefore joins an ecosystem of conceptually new approaches (*77*–*79*) complementary to these more well-established methods.

We expect that improvements to IGS will further enable the study of genome sequence, structure, and function. In addition to the cultured cells and early embryos presented here, we anticipate extension of IGS to a broader range of cell types and intact tissues. Outside of development, IGS may be well suited to studying cancers, in particular, investigations into how copy number instability and translocations contribute to tumor heterogeneity and alter nuclear morphology (*80*). The transposase-based library construction used in IGS may also be extended to measure the spatial localization of the accessible genome (*30*, *81*). Further, because nuclear volume is the primary constraint on the amplicon yield of IGS, we anticipate many-fold improvements in yield and resolution, either through smaller amplicons (*82*) or (preferably) through integration of IGS with expansion microscopy (*83*, *84*), which simultaneously increases nuclear volume by 50- to 100-fold and enables superresolved imaging by physical expansion of samples. Finally, after our proof-of-concept integration with immunostaining, we expect that increasingly multiplexed multiomic (*85*) variations of IGS will be possible. We anticipate that IGS will be instrumental in unifying genomics and microscopy, and therefore sequence and structure.

Methods summary

Library construction

Cells were grown and fixed on glass coverslips, and embryos were fixed in solution and immobilized in polyacrylamide gel in a six-well plate. Phosphorylated DNA adapters were inserted into fixed genomic DNA in situ by incubating samples for 1 hour (cells) or overnight (embryos) with transposase. Hairpins were hybridized to the adapters on either side of the insert, and the complex was circularized by gap-fill ligation. Hairpins contained either a UMI and primers for in situ and ex situ sequencing or a rolling circle amplification (RCA) primer hybridization site. RCA primers were hybridized and RCA was performed overnight, with aminoallyl–2′-deoxyuridine 5′-triphosphate spiked into the reaction. Amplicons were cross-linked by reacting with BS(PEG)9.

In situ sequencing

For cells, the coverslip was mounted in a flow cell, and in situ sequencing reactions were performed using automated fluidics. For embryos, reactions were performed manually in a six-well plate. Samples were treated with calf intestinal phosphatase before the first primer hybridization and before each cleavage reaction. In situ sequencing was performed using sequencing-by-ligation chemistry. Samples were exchanged into an imaging buffer after each round of sequencing. Images were acquired using confocal microscopy. Immunostaining and immunofluorescence imaging were performed after in situ sequencing.

Ex situ sequencing

Samples were transferred into solution and used as input to a polymerase chain reaction. The resulting library was sequenced using high-throughput paired-end sequencing and then aligned to hg38 for PGP1f and mm10 for the early mouse embryos. Aligned reads that overlapped alleles that differed between the B6C3F1 and B6D2F1 strains were annotated as haplotype informative.

Computational integration of in situ and ex situ sequencing data

In situ and ex situ sequencing data were computationally integrated using a probabilistic UMI-matching approach that borrows principles from single-bit error correction to account for signal intermingling between densely packed amplicons, as well as the decay of sequencing quality over successive rounds of in situ sequencing.

Detailed methods for sample preparation, library construction, multimodal sequencing, imaging, image analysis, and all data analyses are described in the materials and methods section of the supplementary materials. Oligonucleotide sequences are provided in table S4. A description of methods for kit-free synthesis of in situ sequencing reagents is given in the supplementary text and in tables S5 and S6. A description of cost, complexity, and throughput of the method is found in the supplementary text and in table S7.

REFERENCES AND NOTES

1. B. Bonev, G. Cavalli, Organization and function of the 3D genome. *Nat. Rev. Genet.* **17**, 661–678 (2016). doi: 10.1038/nrg.2016.112; pmid: 27739532
2. M. J. Rowley, V. G. Corces, Organizational principles of 3D genome architecture. *Nat. Rev. Genet.* **19**, 789–800 (2018). doi: 10.1038/s41576-018-0060-8; pmid: 30367165
3. H. Zheng, W. Xie, The role of 3D genome organization in development and cell differentiation. *Nat. Rev. Mol. Cell Biol.* **20**, 535–550 (2019). doi: 10.1038/s41580-019-0132-4; pmid: 31197269
4. M. Spielmann, D. G. Lupiáñez, S. Mundlos, Structural variation in the 3D genome. *Nat. Rev. Genet.* **19**, 453–467 (2018). doi: 10.1038/s41576-018-0007-0; pmid: 29692413
5. J. Dekker, K. Rippe, M. Dekker, N. Kleckner, Capturing chromosome conformation. *Science* **295**, 1306–1311 (2002). doi: 10.1126/science.1067799; pmid: 11847345
6. E. Lieberman-Aiden *et al*., Comprehensive mapping of long-range interactions reveals folding principles of the human genome. *Science* **326**, 289–293 (2009). doi: 10.1126/science.1181369; pmid: 19815776
7. J. M. Levsky, R. H. Singer, Fluorescence in situ hybridization: Past, present and future. *J. Cell Sci.* **116**, 2833–2838 (2003). doi: 10.1242/jcs.00633; pmid: 12808017
8. J. R. Dixon *et al*., Topological domains in mammalian genomes identified by analysis of chromatin interactions. *Nature* **485**, 376–380 (2012). doi: 10.1038/nature11082; pmid: 22495300
9. T. Sexton *et al*., Three-dimensional folding and functional organization principles of the *Drosophila* genome. *Cell* **148**, 458–472 (2012). doi: 10.1016/j.cell.2012.01.010; pmid: 22265598
10. S. S. P. Rao *et al*., A 3D map of the human genome at kilobase resolution reveals principles of chromatin looping. *Cell* **159**, 1665–1680 (2014). doi: 10.1016/j.cell.2014.11.021; pmid: 25497547
11. E. P. Nora *et al*., Spatial partitioning of the regulatory landscape of the X-inactivation centre. *Nature* **485**, 381–385 (2012). doi: 10.1038/nature11049; pmid: 22495304
12. R. Kalhor, H. Tjong, N. Jayathilaka, F. Alber, L. Chen, Genome architectures revealed by tethered chromosome conformation capture and population-based modeling. *Nat. Biotechnol.* **30**, 90–98 (2011). doi: 10.1038/nbt.2057; pmid: 22198700
13. T. Nagano *et al*., Single-cell Hi-C reveals cell-to-cell variability in chromosome structure. *Nature* **502**, 59–64 (2013). doi: 10.1038/nature12593; pmid: 24067610
14. T. Nagano *et al*., Cell-cycle dynamics of chromosomal organization at single-cell resolution. *Nature* **547**, 61–67 (2017). doi: 10.1038/nature23001; pmid: 28682332
15. V. Ramani *et al*., Massively multiplex single-cell Hi-C. *Nat. Methods* **14**, 263–266 (2017). doi: 10.1038/nmeth.4155; pmid: 28135255
16. T. J. Stevens *et al*., 3D structures of individual mammalian genomes studied by single-cell Hi-C. *Nature* **544**, 59–64 (2017). doi: 10.1038/nature21429; pmid: 28289288
17. L. Tan, D. Xing, C.-H. Chang, H. Li, X. S. Xie, Three-dimensional genome structures of single diploid human cells. *Science* **361**, 924–928 (2018). doi: 10.1126/science.aat5641; pmid: 30166492
18. T. Cremer, M. Cremer, Chromosome territories. *Cold Spring Harb. Perspect. Biol.* **2**, a003889 (2010). doi: 10.1101/cshperspect.a003889; pmid: 20300217
19. J. Fraser, I. Williamson, W. A. Bickmore, J. Dostie, An Overview of Genome Organization and How We Got There: From FISH to Hi-C. *Microbiol. Mol. Biol. Rev.* **79**, 347–372 (2015). doi: 10.1128/MMBR.00006-15; pmid: 26223848
20. S. Wang *et al*., Spatial organization of chromatin domains and compartments in single chromosomes. *Science* **353**, 598–602 (2016). doi: 10.1126/science.aaf8084; pmid: 27445307
21. D. I. Cattoni *et al*., Single-cell absolute contact probability detection reveals chromosomes are organized by multiple low-frequency yet specific interactions. *Nat. Commun.* **8**, 1753 (2017). doi: 10.1038/s41467-017-01962-x; pmid: 29170434
22. B. Bintu *et al*., Super-resolution chromatin tracing reveals domains and cooperative interactions in single cells. *Science* **362**, eaau1783 (2018). doi: 10.1126/science.aau1783; pmid: 30361340
23. G. Nir *et al*., Walking along chromosomes with super-resolution imaging, contact maps, and integrative modeling. *PLOS Genet.* **14**, e1007872 (2018). doi: 10.1371/journal.pgen.1007872; pmid: 30586358
24. Q. Szabo *et al*., TADs are 3D structural units of higher-order chromosome organization in *Drosophila*. *Sci. Adv.* **4**, eaar8082 (2018). doi: 10.1126/sciadv.aar8082; pmid: 29503869
25. E. H. Finn *et al*., Extensive heterogeneity and intrinsic variation in spatial genome organization. *Cell* **176**, 1502–1515.e10 (2019). doi: 10.1016/j.cell.2019.01.020; pmid: 30799036
26. L. J. Mateo *et al*., Visualizing DNA folding and RNA in embryos at single-cell resolution. *Nature* **568**, 49–54 (2019). doi: 10.1038/s41586-019-1035-4; pmid: 30886393
27. A. M. Cardozo Gizzi *et al*., Microscopy-based chromosome conformation capture enables simultaneous visualization of genome organization and transcription in intact organisms. *Mol. Cell* **74**, 212–222.e5 (2019). doi: 10.1016/j.molcel.2019.01.011; pmid: 30795893
28. B. J. Beliveau *et al*., Single-molecule super-resolution imaging of chromosomes and in situ haplotype visualization using Oligopaint FISH probes. *Nat. Commun.* **6**, 7147 (2015). doi: 10.1038/ncomms8147; pmid: 25962338
29. Materials and methods are available as supplementary materials.
30. X. Chen *et al*., ATAC-see reveals the accessible genome by transposase-mediated imaging and sequencing. *Nat. Methods* **13**, 1013–1020 (2016). doi: 10.1038/nmeth.4031; pmid: 27749837
31. J. H. Lee *et al*., Highly multiplexed subcellular RNA sequencing in situ. *Science* **343**, 1360–1363 (2014). doi: 10.1126/science.1250212; pmid: 24578530
32. J. R. Moffitt *et al*., High-throughput single-cell gene-expression profiling with multiplexed error-robust fluorescence in situ hybridization. *Proc. Natl. Acad. Sci. U.S.A.* **113**, 11046–11051 (2016). doi: 10.1073/pnas.1612826113; pmid: 27625426
33. E. V. Volpi *et al*., Large-scale chromatin organization of the major histocompatibility complex and other regions of human

chromosome 6 and its response to interferon in interphase nuclei. *J. Cell Sci.* **113**, 1565–1576 (2000). pmid: 10751148

34. A. Bolzer *et al*., Three-dimensional maps of all chromosomes in human male fibroblast nuclei and prometaphase rosettes. *PLOS Biol.* **3**, e157 (2005). doi: 10.1371/journal.pbio.0030157; pmid: 15839726
35. A. P. J. de Koning, W. Gu, T. A. Castoe, M. A. Batzer, D. D. Pollock, Repetitive elements may comprise over two-thirds of the human genome. *PLOS Genet.* **7**, e1002384 (2011). doi: 10.1371/journal.pgen.1002384; pmid: 22144907
36. K. H. Miga *et al*., Telomere-to-telomere assembly of a complete human X chromosome. *Nature* **585**, 79–84 (2020). doi: 10.1038/s41586-020-2547-7; pmid: 32663838
37. A. Cournac, R. Koszul, J. Mozziconacci, The 3D folding of metazoan genomes correlates with the association of similar repetitive elements. *Nucleic Acids Res.* **44**, 245–255 (2016). doi: 10.1093/nar/gkv1292; pmid: 26609133
38. V. Casa, D. Gabellini, A repetitive elements perspective in Polycomb epigenetics. *Front. Genet.* **3**, 199 (2012). doi: 10.3389/fgene.2012.00199; pmid: 23060903
39. M. Hausmann, J.-H. Lee, A. Sievers, M. Krufczik, G. Hildenbrand, COMBinatorial Oligonucleotide FISH (COMBO-FISH) with uniquely binding repetitive DNA probes. *Methods Mol. Biol.* **2175**, 65–77 (2020). doi: 10.1007/978-1-0716-0763-3_6; pmid: 32681484
40. W. Bao, K. K. Kojima, O. Kohany, Repbase Update, a database of repetitive elements in eukaryotic genomes. *Mob. DNA* **6**, 11 (2015). doi: 10.1186/s13100-015-0041-9; pmid: 26045719
41. M. Falk *et al*., Heterochromatin drives compartmentalization of inverted and conventional nuclei. *Nature* **570**, 395–399 (2019). doi: 10.1038/s41586-019-1275-3; pmid: 31168090
42. H. Muller, J. Gil Jr., I. A. Drinnenberg, The impact of centromeres on spatial genome architecture. *Trends Genet.* **35**, 565–578 (2019). doi: 10.1016/j.tig.2019.05.003; pmid: 31200946
43. C. B. Hug, J. M. Vaquerizas, The birth of the 3D genome during early embryonic development. *Trends Genet.* **34**, 903–914 (2018). doi: 10.1016/j.tig.2018.09.002; pmid: 30292539
44. C. Chazaud, Y. Yamanaka, Lineage specification in the mouse preimplantation embryo. *Development* **143**, 1063–1074 (2016). doi: 10.1242/dev.128314; pmid: 27048685
45. S. H. Namekawa, B. Payer, K. D. Huynh, R. Jaenisch, J. T. Lee, Two-step imprinted X inactivation: Repeat versus genic silencing in the mouse. *Mol. Cell. Biol.* **30**, 3187–3205 (2010). doi: 10.1128/MCB.00227-10; pmid: 20404085
46. M. Borsos *et al*., Genome-lamina interactions are established de novo in the early mouse embryo. *Nature* **569**, 729–733 (2019). doi: 10.1038/s41586-019-1233-0; pmid: 31118510
47. I. M. Flyamer *et al*., Single-nucleus Hi-C reveals unique chromatin reorganization at oocyte-to-zygote transition. *Nature* **544**, 110–114 (2017). doi: 10.1038/nature21711; pmid: 28355183
48. Z. Du *et al*., Allelic reprogramming of 3D chromatin architecture during early mammalian development. *Nature* **547**, 232–235 (2017). doi: 10.1038/nature23263; pmid: 28703188
49. Y. Ke *et al*., 3D chromatin structures of mature gametes and structural reprogramming during mammalian embryogenesis. *Cell* **170**, 367–381.e20 (2017). doi: 10.1016/j.cell.2017.06.029; pmid: 28709003
50. S. Collombet *et al*., Parental-to-embryo switch of chromosome organization in early embryogenesis. *Nature* **580**, 142–146 (2020). doi: 10.1038/s41586-020-2125-z; pmid: 32238933
51. M.-E. Torres-Padilla, D.-E. Parfitt, T. Kouzarides, M. Zernicka-Goetz, Histone arginine methylation regulates pluripotency in the early mouse embryo. *Nature* **445**, 214–218 (2007). doi: 10.1038/nature05458; pmid: 17215844
52. A. Burton *et al*., Single-cell profiling of epigenetic modifiers identifies PRDM14 as an inducer of cell fate in the mammalian embryo. *Cell Rep.* **5**, 687–701 (2013). doi: 10.1016/j.celrep.2013.09.044; pmid: 24183668
53. A. Burton, M.-E. Torres-Padilla, Chromatin dynamics in the regulation of cell fate allocation during early embryogenesis. *Nat. Rev. Mol. Cell Biol.* **15**, 723–735 (2014). doi: 10.1038/nrm3885; pmid: 25303116
54. T. Aguirre-Lavin *et al*., 3D-FISH analysis of embryonic nuclei in mouse highlights several abrupt changes of nuclear organization during preimplantation development. *BMC Dev. Biol.* **12**, 30 (2012). doi: 10.1186/1471-213X-12-30; pmid: 23095683
55. H. Fulka, F. Aoki, Nucleolus precursor bodies and ribosome biogenesis in early mammalian embryos: Old theories and new discoveries. *Biol. Reprod.* **94**, 143 (2016). doi: 10.1095/biolreprod.115.136093; pmid: 26935600
56. W. Mayer, A. Smith, R. Fundele, T. Haaf, Spatial separation of parental genomes in preimplantation mouse embryos. *J. Cell Biol.* **148**, 629–634 (2000). doi: 10.1083/jcb.148.4.629; pmid: 10684246
57. J. Reichmann *et al*., Dual-spindle formation in zygotes keeps parental genomes apart in early mammalian embryos. *Science* **361**, 189–193 (2018). doi: 10.1126/science.aar7462; pmid: 30002254
58. C. R. Cowan, P. M. Carlton, W. Z. Cande; Rabl Organization and the Bouquet, The polar arrangement of telomeres in interphase and meiosis. Rabl organization and the bouquet. *Plant Physiol.* **125**, 532–538 (2001). doi: 10.1104/pp.125.2.532; pmid: 11161011
59. M. Pouokam *et al*., The Rabl configuration limits topological entanglement of chromosomes in budding yeast. *Sci. Rep.* **9**, 6795 (2019). doi: 10.1038/s41598-019-42967-4; pmid: 31043625
60. M. T. Lee, A. R. Bonneau, A. J. Giraldez, Zygotic genome activation during the maternal-to-zygotic transition. *Annu. Rev. Cell Dev. Biol.* **30**, 581–613 (2014). doi: 10.1146/annurev-cellbio-100913-013027; pmid: 25150012
61. K. Ahmed *et al*., Global chromatin architecture reflects pluripotency and lineage commitment in the early mouse embryo. *PLOS ONE* **5**, e10531 (2010). doi: 10.1371/journal.pone.0010531; pmid: 20479880
62. N. Plachta, T. Bollenbach, S. Pease, S. E. Fraser, P. Pantazis, Oct4 kinetics predict cell lineage patterning in the early mammalian embryo. *Nat. Cell Biol.* **13**, 117–123 (2011). doi: 10.1038/ncb2154; pmid: 21258368
63. K. Piotrowska-Nitsche, A. Perea-Gomez, S. Haraguchi, M. Zernicka-Goetz, Four-cell stage mouse blastomeres have different developmental properties. *Development* **132**, 479–490 (2005). doi: 10.1242/dev.01602; pmid: 15634695
64. J. Walter, L. Schermelleh, M. Cremer, S. Tashiro, T. Cremer, Chromosome order in HeLa cells changes during mitosis and early G1, but is stably maintained during subsequent interphase stages. *J. Cell Biol.* **160**, 685–697 (2003). doi: 10.1083/jcb.200211103; pmid: 12604593
65. D. Gerlich *et al*., Global chromosome positions are transmitted through mitosis in mammalian cells. *Cell* **112**, 751–764 (2003). doi: 10.1016/S0092-8674(03)00189-2; pmid: 12654243
66. J. Kind *et al*., Single-cell dynamics of genome-nuclear lamina interactions. *Cell* **153**, 178–192 (2013). doi: 10.1016/j.cell.2013.02.028; pmid: 23523135
67. I. Thomson, S. Gilchrist, W. A. Bickmore, J. R. Chubb, The radial positioning of chromatin is not inherited through mitosis but is established de novo in early G1. *Curr. Biol.* **14**, 166–172 (2004). doi: 10.1016/j.cub.2003.12.024; pmid: 14738741
68. C.-S. Lee *et al*., Chromosome position determines the success of double-strand break repair. *Proc. Natl. Acad. Sci. U.S.A.* **113**, E146–E154 (2016). doi: 10.1073/pnas.1523660113; pmid: 26715752
69. E. R. Phillips, P. J. McKinnon, DNA double-strand break repair and development. *Oncogene* **26**, 7799–7808 (2007). doi: 10.1038/sj.onc.1210877; pmid: 18066093
70. E. Vanneste *et al*., Chromosome instability is common in human cleavage-stage embryos. *Nat. Med.* **15**, 577–583 (2009). doi: 10.1038/nm.1924; pmid: 19396175
71. Y. Zhang *et al*., Spatial organization of the mouse genome and its role in recurrent chromosomal translocations. *Cell* **148**, 908–921 (2012). doi: 10.1016/j.cell.2012.02.002; pmid: 22341456
72. J. M. Engreitz, V. Agarwala, L. A. Mirny, Three-dimensional genome architecture influences partner selection for chromosomal translocations in human disease. *PLOS ONE* **7**, e44196 (2012). doi: 10.1371/journal.pone.0044196; pmid: 23028501
73. H. Q. Nguyen *et al*., 3D mapping and accelerated super-resolution imaging of the human genome using in situ sequencing. *Nat. Methods* **17**, 822–832 (2020). doi: 10.1038/s41592-020-0890-0; pmid: 32719531
74. J.-H. Su, P. Zheng, S. S. Kinrot, B. Bintu, X. Zhuang, Genome-scale imaging of the 3D organization and transcriptional activity of chromatin. *Cell* **182**, 1641–1659.e26 (2020). doi: 10.1016/j.cell.2020.07.032; pmid: 32822575
75. J. M. Luppino *et al*., Cohesin promotes stochastic domain intermingling to ensure proper regulation of boundary-proximal genes. *Nat. Genet.* **52**, 840–848 (2020). doi: 10.1038/s41588-020-0647-9; pmid: 32572210
76. B. D. Fields, S. C. Nguyen, G. Nir, S. Kennedy, A multiplexed DNA FISH strategy for assessing genome architecture in *Caenorhabditis elegans*. *eLife* **8**, e42823 (2019). doi: 10.7554/eLife.42823; pmid: 31084706
77. R. A. Beagrie *et al*., Complex multi-enhancer contacts captured by genome architecture mapping. *Nature* **543**, 519–524 (2017). doi: 10.1038/nature21411; pmid: 28273065
78. S. A. Quinodoz *et al*., Higher-order inter-chromosomal hubs shape 3D genome organization in the nucleus. *Cell* **174**, 744–757.e24 (2018). doi: 10.1016/j.cell.2018.05.024; pmid: 29887377
79. G. Girelli *et al*., GPSeq reveals the radial organization of chromatin in the cell nucleus. *Nat. Biotechnol.* **38**, 1184–1193 (2020). pmid: 32451505
80. D. Zink, A. H. Fischer, J. A. Nickerson, Nuclear structure in cancer cells. *Nat. Rev. Cancer* **4**, 677–687 (2004). doi: 10.1038/nrc1430; pmid: 15343274
81. J. D. Buenrostro, P. G. Giresi, L. C. Zaba, H. Y. Chang, W. J. Greenleaf, Transposition of native chromatin for fast and sensitive epigenomic profiling of open chromatin, DNA-binding proteins and nucleosome position. *Nat. Methods* **10**, 1213–1218 (2013). doi: 10.1038/nmeth.2688; pmid: 24097267
82. C.-M. Clausson *et al*., Compaction of rolling circle amplification products increases signal integrity and signal-to-noise ratio. *Sci. Rep.* **5**, 12317 (2015). doi: 10.1038/srep12317; pmid: 26202090
83. F. Chen, P. W. Tillberg, E. S. Boyden, Optical imaging. Expansion microscopy. *Science* **347**, 543–548 (2015). doi: 10.1126/science.1260088; pmid: 25592419
84. S. Alon *et al*., Expansion sequencing: Spatially precise in situ transcriptomics in intact biological systems. *Science* **371**, eaax2656 (2021). doi: 10.1126/science.aax2656; pmid: 33509999
85. C. Zhu, S. Preissl, B. Ren, Single-cell multimodal omics: The power of many. *Nat. Methods* **17**, 11–14 (2020). doi: 10.1038/s41592-019-0691-5; pmid: 31907462
86. E. Williams *et al*., The Image Data Resource: A bioimage data integration and publication platform. *Nat. Methods* **14**, 775–781 (2017). doi: 10.1038/nmeth.4326; pmid: 28775673
87. A. C. Payne, Z. D. Chiang, P. L. Reginato, S. M. Mangiameli, zchiang/in_situ_genome_sequencing_processing: In situ genome sequencing processing code for: In situ genome sequencing resolves DNA sequence and structure in intact biological samples, Version 1.02, Zenodo (2020); https://doi.org/10.5281/zenodo.4299227.
88. A. C. Payne, Z. D. Chiang, P. L. Reginato, zchiang/in_situ_genome_sequencing_analysis: In situ genome sequencing analysis code for: In situ genome sequencing resolves DNA sequence and structure in intact biological samples, Version 1.0, Zenodo (2020); https://doi.org/10.5281/zenodo.4299125.

ACKNOWLEDGMENTS

We thank members of the Church, Boyden, Buenrostro, and Chen laboratories for useful discussions; S. Alon, R. Kalhor, D. Lee, M. Villanueva, M. Aryee, T. Zhao, P. Wiggins, W. Xie, B. Zhang, T. Wu, and E. Lieberman-Aiden for useful suggestions; and J. Strecker for purified Tn5 transposase. **Funding:** J.D.B. and F.C. were supported by an Allen Institute Distinguished Investigator award and NIH R21HG009749. F.C. was also supported by NIH DP5OD024583. E.S.B. was supported by J. Doerr, L. Yang, the Open Philanthropy Project, NIH 1R01NS087950, NIH 1RM1HG008525, NIH 1R01DA045549, NIH 2R01DA029639, NIH 1R01NS102727, NIH UF1NS107697, NIH 1U19MH114821, NIH 1R01EB024261, NIH 1R01MH110932, HHMI, the HHMI–Simons Faculty Scholars Program, IARPA D16PC00008, the U.S. Army Research Laboratory and the U.S. Army Research Office under contract/grant W911NF1510548, U.S.–Israel Binational Science Foundation grant 2014509, and NIH Director's Pioneer Award 1DP1NS087724. R.J. was supported by NIH R37 CA084198 and R01 MH104610-20. G.M.C. was supported by NIH RM1HG008525. A.C.P. and P.L.R. were supported by NSERC PGS-D awards. Z.D.C. was supported by NHGRI training grant T32HG002295 and the Harvard Quantitative Biology Initiative. **Author contributions:** A.C.P. and P.L.R. developed the protocol and performed experiments. Z.D.C. developed the computational processing pipeline. A.C.P., Z.D.C., P.L.R., S.M.M., J.D.B., and F.C. performed analyses. E.M.M., C.-C.Y., and A.S.L. performed supplementary experiments. S.M. performed embryo preparation under the supervision of R.J. A.S.E. designed the interactive Shiny app. A.C.P., Z.D.C., P.L.R., E.S.B., J.D.B., and F.C. wrote the manuscript with input from all authors. G.M.C., E.S.B., J.D.B., and F.C. supervised the study. **Competing interests:** A.C.P., P.L.R., E.S.B., J.D.B., and F.C. are inventors on patent application 16/043,950 submitted by Harvard College and

Massachusetts Institute of Technology, which covers IGS technology. J.D.B. holds patents related to ATAC-seq and is on the scientific advisory board for Camp4, Seqwell, and Celsee. F.C. is a paid consultant for Celsius Therapeutics. G.M.C. is a cofounder and SAB member of ReadCoor and is an adviser to 10x Genomics after their acquisition of ReadCoor. Conflict of interest link for G.M.C.: http://arep.med.harvard.edu/gmc/tech.html. R.J. is an adviser for and cofounder of Fate Therapeutics, Fulcrum Therapeutics, Omega Therapeutics, and Dewpoint Therapeutics. **Data and materials availability:** Raw sequencing data are available from the Sequence Read Archive (SRA) under accession nos. SRR12938556 (PGP1f) and SRR12950073 (mouse embryo). Raw images are available from the Image Data Resource (https://idr.openmicroscopy.org) under accession no. idr0101 (*86*). Code for image processing and computational integration of in situ and ex situ sequencing data are available in a Zenodo repository (*87*) and a Github repository (https://github.com/zchiang/in_situ_genome_sequencing_processing/). Code to reproduce the analyses in this manuscript is available in a Zenodo repository (*88*) and a Github repository (https://github.com/zchiang/in_situ_genome_sequencing_analysis/). Hi-C data for PGP1f are available from the Gene Expression Omnibus (GEO) under accession no. GSE12355. Hi-C data from early mouse embryos are available from GEO accession no. GSE82185. DamID data from early mouse embryos are available from GEO accession no. GSE112551. Genotypes for the B6C3F1 and B6D2F1 strains are available from the Mouse Genomes Project (https://www.sanger.ac.uk/data/mouse-genomes-project/). Mouse whole-genome sequencing data are available from SRA accession no. SRR7511358.

SUPPLEMENTARY MATERIALS

science.sciencemag.org/content/371/6532/eaay3446/suppl/DC1
Materials and Methods
Supplementary Text
Figs. S1 to S27
Tables S1 to S7
References (*89*–*101*)
Movies S1 to S5
MDAR Reproducibility Checklist

View/request a protocol for this paper from *Bio-protocol*.

19 June 2019; resubmitted 17 August 2020
Accepted 14 December 2020
Published online 31 December 2020
10.1126/science.aay3446

Science

In situ genome sequencing resolves DNA sequence and structure in intact biological samples

Andrew C. Payne, Zachary D. Chiang, Paul L. Reginato, Sarah M. Mangiameli, Evan M. Murray, Chun-Chen Yao, Styliani Markoulaki, Andrew S. Earl, Ajay S. Labade, Rudolf Jaenisch, George M. Church, Edward S. Boyden, Jason D. Buenrostro and Fei Chen

Science **371** (6532), eaay3446.
DOI: 10.1126/science.aay3446originally published online December 31, 2020

Visualizing the 3D genome in situ

The conformation of the genome within the cell changes depending on cell state, such that being able to visualize genome structure can identify cis and trans interactions among regulatory genetic elements. Payne *et al.* have developed an unbiased genome-sequencing technique in single cells in situ that can infer the chromatin structure by imaging. They were able to identify sequences at subnuclei locations to analyze the proximity relationships among genetic elements within and across chromosomes in single cells. Using this technique, they could detect chromosome territories and distinctions between different types of repetitive sequences and chromosomal features. This method can map and image genomic coordinates with submicrometer resolution in intact single cells.

Science, this issue p. eaay3446

Science (print ISSN 0036-8075; online ISSN 1095-9203) is published by the American Association for the Advancement of Science, 1200 New York Avenue NW, Washington, DC 20005. The title *Science* is a registered trademark of AAAS.